Accurate and precise ab initio anharmonic free-energy calculations for metallic crystals: Application to hcp Fe at high temperature and pressure

Sabry G. Moustafa, Andrew J. Schultz, Eva Zurek, and David A. Kofke

Phys. Rev. B **96**, 014117 — Published 26 July 2017

DOI: 10.1103/PhysRevB.96.014117

Accurate and precise *ab initio* anharmonic free-energy calculations for metallic crystals. Application to hcp Fe at high temperature and pressure

Sabry G. Moustafa,[1] Andrew J. Schultz,[1] Eva Zurek,[2] and David A. Kofke[1,*]

[1] *Department of Chemical and Biological Engineering, University at Buffalo, The State University of New York, Buffalo, New York 14260-4200, USA*

[2] *Department of Chemistry, University at Buffalo, The State University of New York, Buffalo, New York 14260-3000, USA*

A framework for computing the anharmonic free energy (FE) of metallic crystals using Born-Oppenheimer *ab initio* molecular dynamics (AIMD) simulation, with unprecedented efficiency, is introduced and demonstrated for the hcp phase of iron at extreme conditions (up to ≈ 290 GPa and 5000 K). The advances underlying this work are: (1) A recently introduced harmonically-mapped averaging temperature integration (HMA-TI) method reduces the computational cost by order(s) of magnitude compared to the conventional TI approach. The TI path starts from zero Kelvin, where it assumes the behavior is given exactly by a harmonic treatment; this feature restricts application to systems that have no imaginary phonons in this limit. (2) A Langevin thermostat with the HMA-TI method allows use of a relatively large MD time step (4 fs, which is about eight times larger than the size needed for the Andersen thermostat) without loss of accuracy. (3) AIMD sampling is accelerated by using density functional theory (DFT) with a low-level parameter set, then the measured quantities of selected configurations are robustly reweighted to a higher level of DFT. This introduces a speedup of about 20-30× compared to directly simulating the accurate system. (4a) The temperature (T) dependence of the hcp equilibrium shape (i.e. c/a axial ratio) is determined (including anharmonicity), with uncertainty less than ±0.001. (4b) Electronic excitation is included through Mermin's finite-temperature extension of the $T = 0$ K DFT. A simple FE perturbation method is introduced to handle the difficulty associated with applying the TI method with a T-dependent geometry and (due to electronic excitation) potential-energy surface. (5) The FE in the thermodynamic limit is attained through extrapolation of only the (computationally inexpensive) quasiharmonic FE, because the anharmonic FE contribution has negligible finite-size effects. All methods introduced here do not affect the AIMD sampling – results are obtained through post-processing — so established AIMD codes can be employed without modification. Analytical formulas fitted to the results for the variation of the equilibrium c/a ratio and FE components with T are provided. Notably, effects of magnetic excitations are not included, and may yet prove important to the overall FE; if so, it is plausible that such contributions can be added perturbatively to the FE values reported here. Notwithstanding these considerations, FE values are obtained with an estimated accuracy and precision of 2 meV/atom, suggesting that the capability to compute the phase diagram of iron at Earth's inner core conditions is within reach.

I. INTRODUCTION

The ability to quickly (but robustly) predict the crystal structure of an atomistic system is one of the leading goals in modern computational science[1–9]. Reaching this target would allow for the study of a huge number of polymorphs first on the computer, where stable candidates can be identified for synthesis in the laboratory. Alternatively, crystal-structure calculations can be used to probe behavior that is inaccessible to experiment. A prominent example is behavior at conditions found at the Earth's inner core. The Earth's core is composed primarily of iron, with about 10% nickel and a number of light impurities, such as sulfur, oxygen, silicon, carbon, and hydrogen that are likely to be present[10–12] (it has even been proposed that the "missing xenon paradox" can be explained via reactions of Xe with Fe and Ni at inner-core conditions[13]). An outstanding problem is determination of the structure of the core material—among other things, this knowledge can inform theories of the Earth's evolution, aid understanding of its physical features (e.g., magnetic, gravitational fields), and guide interpretation of seismological measurements. The study of pure iron is a useful starting point in approaching this question.

The free energy (FE) is the pivotal thermodynamic quantity needed for crystal-structure analysis, because the globally stable structure is the one with the lowest FE. For a system of N atoms, at a temperature T, occupying a d-dimensional space of volume V, the Helmholtz FE $A(T,V)$ (apart from the ideal gas contribution) is related to the configurational canonical partition function Z[14],

$$Z\left(T,V\right)=\int_{V}e^{-\beta U(\mathbf{x})}d\mathbf{x}, \tag{1a}$$

through

$$A\left(T,V\right)=-k_{\mathrm{B}}T\ln Z\left(T,V\right), \tag{1b}$$

where $\beta = 1/k_{\mathrm{B}}T$, k_{B} is the Boltzmann constant, and $U(\mathbf{x})$ is the system intermolecular potential energy as a function of the dN coordinates represented by $\mathbf{x}$.

Building accurate phase diagrams from the FE as computed using first-principles models is not trivial, and still far from being routinely achieved using the current

methods and resources. The main reason for this difficulty is the need to perform *ab initio* molecular dynamics (AIMD) simulations to evaluate the configurational integral defining Z. AIMD calculations are very demanding, as thousands of molecular dynamics steps — each potentially taking hours of computational effort — are normally needed to get precise data. This is particularly a challenge for metals as a much higher quality (compared to insulators) of density functional theory (DFT) parameters is needed to treat electronic excitation (especially at low temperature). Moreover, the FE calculation *per se* has complications of its own that compound the computational burden[15–17]. Consequently, approximate FE methods are often employed.

The most elementary estimate of the FE approximates it using just the lattice (or static) energy, ignoring entropic effects entirely. Obviously this approach is ineffective in describing behavior that is driven by changes in temperature, such as most phase transitions. The quasiharmonic (qh) approximation (or lattice dynamics)[18] is often employed to estimate the vibrational (or thermal) contribution of the FE. The advantage of this approach is that the FE is approximated using first-principles methods with entropic contributions included, such as the frozen-phonon[19] or density-functional perturbation theory[20] approaches, but without the need to perform any AIMD simulations. The quasiharmonic treatment has been applied to several systems to investigate thermodynamic stability, but accuracy decreases as atomic vibrations increase in magnitude, compared to the intermolecular spacing. Typically this happens upon approaching the melting point, where anharmonic effects become non-negligible due to phonon-phonon interactions. Moreover, a quasiharmonic treatment fails for systems having imaginary frequencies in the phonon spectrum, which sometimes occurs for systems at $T = 0$ K even though they are dynamically stable at higher temperatures (e.g., high-pressure bcc iron).

Approximate remedies have been introduced to incorporate anharmonicity through temperature renormalization of phonon frequencies (which are T-independent in the quasiharmonic theory). This includes methods like velocity autocorrelation[21–25], average force constants[26–30], variational approaches[31–35], a semiempirical *ansatz*[36–38], and the most commonly used method: self-consistent *ab initio* lattice dynamics (SCAILD)[39]. The general idea in common with these methods is to formulate a temperature-dependent effective harmonic system, defining force constants or the elements of a dynamical matrix, such that some feature of the harmonic system matches that computed in the system being studied, or a formal bound on the target-system FE is minimized. The effective harmonic model so derived then captures elements of anharmonic behavior implicitly; its FE is evaluated as if the harmonic description of noninteracting phonons is valid for all excitations, so it is still tractable. Such approaches have been shown to produce phase diagrams, phonon spectra, etc., that are consistent with the systems being modeled. Nevertheless, they are approximate to some degree, meaning that the FE they yield will not necessarily match the true FE for the PES they are formulated to describe. In most cases, they have not been compared to rigorously evaluated FE values, so it is difficult to know exactly how accurate they are in this respect. Moreover, they cannot be improved systematically, so their accuracy cannot be evaluated by comparing different levels of approximation. Hence, even more rigorous methods are needed to evaluate the FE of crystals as robustly as possible, if only to provide a basis for evaluating methods based on an effective harmonic model. Along these lines, AIMD calculations have been attempted for iron at extreme conditions[40–45], but these efforts have had to use approximations of their own, in the DFT treatment and/or the FE computational method, trading off accuracy to gain useful precision in the result. Due to these challenges associated with *ab initio*-based approaches, classical force-fields and/or theories are often adopted to get an estimate of the FE. However, such compromises diminish predictive capabilities.

In this work we aim to demonstrate that it is now possible to obtain accurate and precise first-principles values for the FE with relatively low computational cost. The key to this capability is the recently introduced harmonically mapped averaging (HMA) method[46–48], described below. HMA does not require harmonic behavior to yield an accurate result; rather, anharmonicity impacts only the efficiency of HMA. However, the FE calculation is based on integration from low temperature, and it is necessary that a harmonic treatment be appropriate there for the method (in the basic form presented here) to be applicable. For the demonstration, we calculate the absolute FE of the high-pressure hcp phase of iron (which is a candidate structure in the Earth's inner core[49]) for a single isochore (7.0 Å^3/atom) up to temperatures near melting (5000 K), with full inclusion of anharmonicity, electronic excitation, and the change of equilibrium c/a ratio with temperature. At the conditions of interest, iron is paramagnetic, and we neglect contributions to the FE from magnetic properties. However, these contributions may be significant relative to the other effects[50]; we discuss this issue more in Sec. V.

We set a target accuracy of 2 meV/atom for our final FE estimate. The basis for this small tolerance is previously established estimates[42,51,52] for the difference in FE between candidate structures over the conditions of relevance to the Earth's core. Put another way, the experimental uncertainty in the coexistence pressure between hcp and fcc is around 30 GPa at conditions near the Earth's inner core state, which (based on quasiharmonic analysis) corresponds to about 4 meV/atom in Gibbs FE difference between them[51]. Inasmuch as our aim is to improve on the accuracy and precision of what is available from experiment, this sets a standard for our calculations.

Remarkably, we are able to report calculations in the thermodynamic limit ($N \to \infty$), which is important because we find that finite-size effects on the FE are very large (≈ 70 meV/atom difference from the infinite limit).

The $N \to \infty$ limit is attainable because the system-size dependence of the anharmonic FE is negligible compared to that of the quasiharmonic reference[53] (note that the lattice energy has no finite-size effects). Hence, using the quasiharmonic FE at the $N \to \infty$ limit (through extrapolation from different system sizes, which are relatively inexpensive computationally) with a finite-system anharmonic contribution can provide an accurate estimate of the total FE in the thermodynamic limit. This is especially useful when applied to DFT-based models where AIMD with "big" system sizes is not tractable, as is the case here.

The strategy used to compute the first-principles FE involves decomposing the total FE into components, each of which can be computed in the way that is the most effective. All energies are computed using electronic DFT. An important element of the overall approach is the use of less accurate DFT models in support of the modeling calculations that yield the FE with the target accuracy. These methods and models are described in the next two sections. Sec. IV presents results, beginning with an investigation of the effect of thermostats on the convergence of the AIMD with respect to the time step. Then, all the finite-system FE components are presented and an estimate of the FE in the thermodynamic limit is provided. Finally, in Sec. V a summary is given along with conclusions about the techniques employed.

II. FORMALISM AND METHODS

For crystalline systems the canonical decomposition of the FE identifies lattice $U^{\rm lat}$, quasiharmonic $A^{\rm qh}$, and anharmonic $A^{\rm ah}$ contributions:

$$A\,(T) = U^{\rm lat}(T) + A^{\rm qh}(T) + A^{\rm ah}(T); \tag{2}$$

the volume dependence is suppressed for clarity of notation. This decomposition presupposes that the quasiharmonic description has no imaginary phonon frequencies, which would indicate instability at that level of description. Systems that are unstable at $T = 0$ K when treated classically may nevertheless be dynamically or thermodynamically stable at conditions of interest, as thermal or quantum fluctuations can introduce stabilizing effects. Equation (2) can still provide a framework for FE calculation in such cases, but it is then necessary to introduce artificial constraints or stabilizing forces to the system; these artifices can then be removed (and the effect on the FE measured) once reaching the condition of interest, where presumably the system is inherently stable. This procedure has been demonstrated, for example, in Ref. 54. Quasiharmonic instability is not a problem in the present work, where we focus on the vibrationally stable[55] hcp phase of iron, but it would be an issue when applying these methods to iron's bcc phase.

Still, two features of the hcp iron system complicate the calculations:

- the geometry of the hcp crystal — as expressed via the c/a axial ratio, which we will represent using the symbol α — varies with thermodynamic state, and with temperature in particular. We denote the equilibrium value for a given temperature as $\alpha_{\rm eq}(T)$. The T dependence of $\alpha_{\rm eq}$ is evaluated as described in Sec. II E.

- electronic excitation in metallic systems (and iron in particular) gives rise to a temperature dependence in the potential-energy surface (PES). The electronic excitation is included throughout this work using the Fermi-Dirac statistics of fermions (electrons), with the electronic temperature, $T_{\rm el}$, set to the ionic temperature, T, at equilibrium.

While these effects make the lattice energy temperature-dependent, they are otherwise not a problem for evaluation of the $U^{\rm lat}$ and $A^{\rm qh}$ contributions, as both can be readily determined for the given geometry and $T_{\rm el}$ (see below); in contrast, the effects significantly complicate the evaluation of $A^{\rm ah}$. The anharmonic FE contribution is evaluated here via thermodynamic integration in T, and formally, these effects contribute to the integrand:

$$\frac{d}{dT}A^{\rm ah}(T;T_{\rm el},\alpha_{\rm eq}) = \left(\frac{\partial A^{\rm ah}}{\partial T}\right)_{T_{\rm el},\alpha} + \left(\frac{\partial A^{\rm ah}}{\partial T_{\rm el}}\right)_{T,\alpha}\frac{dT_{\rm el}}{dT} + \left(\frac{\partial A^{\rm ah}}{\partial \alpha}\right)_{T,T_{\rm el}}\frac{d\alpha}{dT}. \tag{3}$$

The first term, involving differentiation at constant α and $T_{\rm el}$, is straightforward (Sec. II C). For the remaining terms, of course $dT_{\rm el}/dT = 1$, but the other derivatives involving α and $T_{\rm el}$ are not so easy to evaluate. They could be handled if necessary, but it is more expedient to take a different approach: we use constant values $T_{\rm el} = 0$ and $\alpha = \hat{\alpha}$ along the entire integration path (thereby zeroing out last two terms in Eq. (3)), and then evaluate perturbatively the effect on $A^{\rm ah}$ of setting them to their correct values ($T_{\rm el} \to T$ and $\hat{\alpha} \to \alpha_{\rm eq}$). Thus, we decompose the anharmonic FE contribution as follows:

$$A^{\rm ah}(T;\alpha_{\rm eq}) = A_0^{\rm ah}(T;\hat{\alpha}) + A_{0\to\rm el}^{\rm ah}(T;\hat{\alpha}) + A^{\rm ah}\,(T;\hat{\alpha}\to\alpha_{\rm eq})\,. \tag{4}$$

The 0 subscript appearing on some of the terms in Eq. (4) indicates the reference system, for which $T_{\rm el} = 0$ and the axial ratio α is fixed at the value denoted $\hat{\alpha}$. Further, in the 0-system we employ a DFT treatment (described in Sec. III A) that is computationally less expensive but is of insufficient quality to meet our 2 meV/atom accuracy goal. Thus, we first estimate $A^{\rm ah}(T;\alpha_{\rm eq})$ by thermodynamic integration in temperature using the reference 0-system (we will call it "DFT-0"), yielding $A_0^{\rm ah}(T;\hat{\alpha})$. We then add a correction $A_{0\to\rm el}^{\rm ah}(T;\hat{\alpha})$ to introduce the electronic excitation while simultaneously shifting to higher-quality DFT (we will call this "DFT-el"; see Sec. III A)—properties with no subscript refer to this system, or when needed we indicate it as 'el'. Finally, we add a correction $A^{\rm ah}\,(T;\hat{\alpha}\to\alpha_{\rm eq})$ to account

for the difference from the equilibrium α for each temperature; it turns out that this correction is negligible, but we consider it nonetheless (on the other hand, the effect of α on $U^{\rm lat}$ and $A^{\rm qh}$ is significant).

The remainder of this section explains how each term in Eqs. (2) and (4) is evaluated, in turn. Then, in Sec. III we describe additional details about the models and computations, including specification of the DFT parameters used to define the DFT-0 and DFT-el systems.

A. Lattice energy, $U^{\rm lat}(T;\alpha_{\rm eq})$

The lattice energy is defined as the potential energy when all atoms are at their lattice sites $\mathbf{x}^{\rm lat}$ (which is different from the average energy at 0 K, due to quantum zero-point effects). It can be evaluated to high accuracy using a reciprocal-space sum[56], and, assuming a converged sum, there are no finite-size effects per se; hence $U^{\rm lat}$ can be evaluated essentially exactly using only one primitive unit cell. As mentioned above, normally the lattice energy is temperature independent. However, in the present application it has a temperature dependence due to the effect of electronic excitation on the PES, and the temperature-varying c/a ratio (which itself depends on all the FE contributions; the means we use to evaluate $\alpha_{\rm eq}(T)$ is described in Sec. II E).

B. Quasiharmonic FE, $A^{\rm qh}(T;\alpha_{\rm eq})$

The classical quasiharmonic contribution to the FE is

$$A^{\rm qh}(T;\alpha_{\rm eq}) = k_{\rm B}T\sum_j \ln\left(\beta\hbar\omega^{(j)}(T;\alpha_{\rm eq})\right), \qquad (5)$$

where $\hbar \equiv h/2\pi$, with h Planck's constant. The phonon frequencies $\omega^{(j)}$ are obtained as the eigenvalues of the force-constant matrix[18]. We evaluate this for the DFT-el system, hence the $\omega^{(j)}$ depend on the electronic temperature $T_{\rm el}$ (which we equate to T), and $\alpha_{\rm eq}(T)$.

Equation (5) is applicable for temperatures much larger than the Debye temperature, where the nuclei may be treated classically. For highly compressed iron, the Debye temperature is less than 1000 K[57]. Our goal is to calculate the FE near the melting temperature of 5000 K, where a classical treatment should suffice. Accordingly, we use a classical harmonic model (Eq. (5)) and a classical treatment throughout the thermodynamic integration process described in the next section. If we were instead to use a quantum mechanical formulation for $A^{\rm qh}$, then we would need to use a nonclassical treatment also when computing properties for the thermodynamic integration. Assuming the behavior is classical at 5000K, both approaches should give the same result; of course the classical formulation is simpler, but it will give less accurate results at lower temperatures.

C. Thermodynamic integration for $A_0^{\rm ah}(T;\hat{\alpha})$

The first step in the evaluation of $A^{\rm ah}(T;\alpha_{\rm eq})$ is the evaluation of $A_0^{\rm ah}(T;\hat{\alpha})$, and we accomplish this using thermodynamic integration (TI) in temperature. The integration path starts from $T = 0$ K, where the system behaves harmonically (hence $A_0^{\rm ah} = 0$), and proceeds to increasing temperatures while recording averages needed to evaluate the FE at the temperature of interest. The method has been applied to obtain the anharmonic FE of several systems[58–60]. An appealing feature of a T-path is that integration to each point along the path yields the FE at that state. This contrasts with paths based on an unphysical parameter, for which the partial integral usually does not yield a FE applicable to any physically relevant condition[48]. This feature is particularly useful for phase stability analysis where the FE along a wide range of states is required. In addition, we have observed (here and in previous work[46,48]) that the integrand of this method has small curvature along the path; hence, averages at just a few points along the path can be sufficient to yield an accurate result.

Two prerequisites must be satisfied for the TI method to work: (1) the path must be reversible (e.g., no phase transition); (2) the quasiharmonic starting point must have no imaginary frequencies (as discussed above). Although both conditions are satisfied for our system, workarounds can be applied when needed. For example, locating a path in the T/V space having no instability can avoid the former challenge. For the latter, the vibrationally unstable crystal can be (at least for some cases) deformed to another stable polymorph (e.g., using Bain path between fcc and bcc structures[61,62]); alternatively, as discussed above, constraints can be introduced to stabilize the crystal until reaching a condition where it is inherently stable[44,54].

The TI formula for the classical anharmonic contribution is[46]

$$A_0^{\rm ah}(T) = -T\int_0^T \frac{\left\langle U_0^{\rm ah}\right\rangle_0}{\hat{T}^2}d\hat{T}, \qquad (6)$$

where $\left\langle U_0^{\rm ah}\right\rangle_0$ is the ensemble-averaged anharmonic contribution to the energy of the DFT-0 system. Note that the anharmonic FE integrand does not diverge as $\hat{T}\to 0$, because the $\hat{T}^0$ and $\hat{T}^1$ leading terms, corresponding to lattice and quasiharmonic energy contributions, respectively, are absent from $\left\langle U_0^{\rm ah}\right\rangle_0$[48].

We point out again that at sufficiently low temperature, nuclear quantum effects will be relevant, and these need to be reflected in $\left\langle U_0^{\rm ah}\right\rangle_0$ (e.g., by using path integrals, or a semiclassical treatment, perhaps using the classical result as a starting condition). We ignore these considerations here, even though the integral begins at $T = 0$ K and covers low temperatures, because we are targeting the FE calculation to temperatures where these effects are not significant. It is acceptable then to use a purely classical model of DFT-0 as long as we are consistent and use a classical form for $U^{\rm lat}$ (i.e. with no

zero-point energy) and $A^{\rm qh}$ (as done in Eq. (5)).

The anharmonic energy $\langle U_0^{\rm ah}\rangle_0$ must be carefully defined to ensure that it can be measured with good precision while also being consistent with $A^{\rm qh}$ as given by Eq. (5)[48]. Conventional temperature integration (Conv-TI) writes this as

$$\left\langle U_0^{\rm ah}\right\rangle_0 = \langle \Delta U_0\rangle_0 - \frac{d}{2}(N-1)k_{\rm B}T \tag{7}$$

where $\Delta U_0 \equiv U_0(\mathbf{x}) - U_0^{\rm lat}$ and $d(N-1)$ is the total number of degrees of freedom ($d=3$ in this work). This formulation suffers from fluctuations in U_0 that are large in comparison to the difference that forms $\langle U_0^{\rm ah}\rangle$, so it is difficult to evaluate the integrand in Eq. (6) with the necessary precision this way[48]. One might instead subtract a quasiharmonic energy $U_0^{\rm qh}$ evaluated for each configuration, yielding the average $\langle U_0 - U_0^{\rm qh}\rangle_0$. This approach can be useful in other contexts, such as the stochastic self-consistent harmonic approximation method (SSCHA)[33,34]. However it cannot be applied here, because $\langle U_0^{\rm qh}\rangle_0$ is not the same as the average harmonic energy when averaged in the harmonic system, $\langle U_0^{\rm qh}\rangle_{\rm qh}$. Hence, the resulting $\langle U_0^{\rm ah}\rangle$ used in Eq. (6) would yield an $A_0^{\rm ah}$ that is not consistent with Eq. (5) for $A^{\rm qh}$.

As has been discussed elsewhere[46–48], a new harmonic-mapping framework provides a formulation that is still consistent with Eq. (5) while exhibiting much better statistical features:

$$\left\langle U_0^{\rm ah}\right\rangle_0 = \left\langle \Delta U_0 + \frac{1}{2}\,\mathbf{F}_0\cdot\Delta\mathbf{x}\right\rangle_0, \tag{8}$$

where $\mathbf{F}_0$ is the dN-dimensional vector of forces on all atoms, and $\Delta\mathbf{x}$ is the displacement vector of all atoms from their lattice sites $\mathbf{x}^{\rm lat}$. This approach accomplishes a direct measurement of the anharmonic energy for each configuration, which in general is much smaller than the total energy. Consequently, fluctuations are attenuated and the uncertainty in the required ensemble average is much smaller than that possible from Eq. (7) for the same amount of sampling —see Refs. 48 and 46 for more details. The method will be then called "harmonically mapped averaging – temperature integration" (HMA-TI) throughout the study.

D. Correction for DFT model, $A^{\rm ah}_{0\to\rm el}(T;\hat\alpha)$

Having established the anharmonic FE of the DFT-0 model, $A_0^{\rm ah}(T;\hat\alpha)$, we next focus on the difference $A^{\rm ah}_{0\to\rm el}$ needed to obtain the same for the DFT-el model:

$$A^{\rm ah}(T;\hat\alpha) = A_0^{\rm ah}(T;\hat\alpha) + A^{\rm ah}_{0\to\rm el}(T;\hat\alpha). \tag{9}$$

An indirect way to estimate this correction is by measuring the full vibrational, $A^{\rm qh+ah}_{0\to\rm el}$, and quasiharmonic, $A^{\rm qh}_{0\to\rm el}$, corrections separately,

$$A^{\rm ah}_{0\to\rm el}(T;\hat\alpha) = A^{\rm qh+ah}_{0\to\rm el}(T;\hat\alpha) - A^{\rm qh}_{0\to\rm el}(T;\hat\alpha), \tag{10a}$$

The quasiharmonic part can be computed using the standard lattice dynamics as $A^{\rm qh}_{0\to\rm el} = A^{\rm qh} - A_0^{\rm qh}$, while the vibrational correction can be measured using FE perturbation techniques[63], evaluated as an ensemble average taken in the DFT-0 system,

$$A^{\rm qh+ah}_{0\to\rm el}(T;\hat\alpha) = -k_{\rm B}T\ln\left\langle e^{-\beta[\Delta U(\mathbf{x})-\Delta U_0(\mathbf{x})]}\right\rangle_0 \tag{10b}$$

where $\Delta U(\mathbf{x})$ and $\Delta U_0(\mathbf{x})$ are the off-lattice potential energies of configuration $\mathbf{x}$ for the DFT-el and DFT-0 models, respectively.

Alternatively, we can write an expression allowing the anharmonic difference to be obtained directly, using Jarzynski's targeted perturbation framework[64]. A differential form of this idea underlies the HMA expression for $\langle U^{\rm ah}\rangle$ given by Eq. (8), and a discrete version was used by us previously for finite temperature perturbations[54,65]. Instead of Eq. (10), the key equation is

$$A^{\rm ah}_{0\to\rm el}(T;\hat\alpha) = -k_{\rm B}T\ln\left\langle e^{-\beta\left[\Delta U(\mathbf{x}')-\Delta U_0(\mathbf{x})\right]}\right\rangle_0 \tag{11}$$

The crucial difference between these formulations is the coordinate $\mathbf{x}'$ given as the argument to ΔU, which indicates coordinates obtained from $\mathbf{x}$ after performing a mapping. The most suitable mapping would be given in terms of normal-mode coordinates $\eta^{(j)}$ corresponding to the phonon frequencies $\omega^{(j)}$, with the mapping formulated as $\eta'^{(j)} = \eta^{(j)}\omega^{(j)}/\omega_0^{(j)}$. It is more expedient to work with the Cartesian coordinates, scaling the distances from their respective lattice sites by the geometric mean of the frequency ratios:

$$\Delta\mathbf{x}' = \Delta\mathbf{x}\left[\prod_j^{d(N-1)}\frac{\omega^{(j)}}{\omega_0^{(j)}}\right]^{1/d(N-1)} \tag{12}$$

In the general case, Eq. (11) should include a Jacobian term in the average[64]. In the present case, this Jacobian is independent of the configuration, and can be separated from the average. Moreover, for the mapping given by Eq. (12), the Jacobian is $\exp\left(-\beta A^{\rm qh}_{0\to\rm el}\right)$, and its removal from the equation altogether leads us equate the resulting average directly to $A^{\rm ah}_{0\to\rm el}$ in Eq. (11).

After completing calculations using the framework given by Eq. (10), we also implemented the targeted perturbation using the Cartesian coordinate mapping, Eq. (12). The results did not show the expected improvement in performance. As we already had adequate results for $A^{\rm ah}_{0\to\rm el}$ in hand, we did not pursue this further. However a future application may wish to examine whether the targeted perturbation with the normal-mode coordinate mapping offers some advantage for this calculation.

E. Correction for lattice geometry, $A^{\rm ah}(T;\hat{\alpha}\rightarrow\alpha_{\rm eq})$

Combination of Eqs. (6), (9), and (10) leaves us with $A^{\rm ah}(T;\hat{\alpha})$, i.e., DFT-el but with a fixed c/a ratio ($\hat{\alpha}$). We require the FE for the equilibrium geometry, $\alpha_{\rm eq}(T)$, so we need to apply a correction to account for this. Two steps are needed at each temperature: first we must determine $\alpha_{\rm eq}$, then we need to compute the FE difference $A^{\rm ah}\left(T;\hat{\alpha}\rightarrow\alpha_{\rm eq}\right)$ associated with transforming the system from $\hat{\alpha}$ to $\alpha_{\rm eq}$. In principle, the choice of $\hat{\alpha}$ is arbitrary, however the closer the value to $\alpha_{\rm eq}$ the smaller the FE correction. Since we are interested in the high temperature region, a value at 6000 K is used ($\hat{\alpha}=1.6267$, based on minimizing the lat+qh FE with respect to α).

We apply a perturbative approach for both steps. A Taylor expansion for A around $\hat{\alpha}$, performed at constant V and T, yields

$$\delta A=\left.\frac{\partial A}{\partial\alpha}\right|_{\hat{\alpha}}\delta\alpha+\frac{1}{2}\left.\frac{\partial^2 A}{\partial\alpha^2}\right|_{\hat{\alpha}}\delta\alpha^2+... \tag{13}$$

where $\delta A\equiv A\left(\alpha\right)-A\left(\hat{\alpha}\right)$. The equilibrium c/a is then obtained by minimizing δA. Differentiating Eq. (13) with respect to $\delta\alpha$ (keeping only the first- and second-order terms), and then setting the derivative to zero we get,

$$\delta\alpha^{\rm cor}=-\left.\frac{\partial A}{\partial\alpha}\right|_{\hat{\alpha}}\Big/\left.\frac{\partial^2 A}{\partial\alpha^2}\right|_{\hat{\alpha}}. \tag{14}$$

Then $\alpha_{\rm eq}\approx\hat{\alpha}+\delta\alpha^{\rm cor}$. The first FE derivative is directly related to stress anisotropy of the system $\sigma_{\rm aiso}$, which can be measured directly from simulation (with $c/a=\hat{\alpha}$),

$$\left.\frac{\partial A}{\partial\alpha}\right|_{\hat{\alpha}}=\frac{2V}{3\hat{\alpha}}\,\left\langle\sigma_{\rm aiso}\right\rangle, \tag{15}$$

where $\sigma_{\rm aiso}\equiv\sigma_{zz}-0.5\left(\sigma_{xx}+\sigma_{yy}\right)$, with σ_{ii} the diagonal components of the stress tensor. The second derivative is harder to estimate as it would require evaluating the first derivative of $\langle\sigma_{\rm aiso}\rangle$ with respect to α, which is time consuming to determine using AIMD simulation. We use instead the lat+qh description to approximate this derivative. Effectively we assume that the anharmonic stress anisotropy, $\langle\sigma^{\rm ah}_{\rm aiso}\rangle$, is (statistically) independent of c/a around $\hat{\alpha}$ — which is the case here as results (not shown) suggest. Using this approximation, along with Eqs. (14) and (15), our estimate of $\delta\alpha^{\rm cor}$ is given by,

$$\delta\alpha^{\rm cor}=-\frac{2V}{3\hat{\alpha}}\,\frac{\left\langle\sigma_{\rm aiso}\right\rangle}{\left.\partial A^{\rm lat+qh}/\partial\alpha\right|_{\hat{\alpha}}}, \tag{16}$$

where $A^{\rm lat+qh}\equiv U^{\rm lat}+A^{\rm qh}$.

The change in the anharmonic FE accompanying the change in α is again given via the Taylor expansion of Eq. (13), but applied specifically to the anharmonic component of the FE. We have already assumed in deriving Eq. (16) that $\partial^2 A^{\rm ah}/\partial\alpha^2=0$, so we use a first-order expansion. The result may be expressed

$$A^{\rm ah}\left(T;\hat{\alpha}\rightarrow\alpha_{\rm eq}\right)=-\left(\frac{2V}{3\hat{\alpha}}\right)^2\,\frac{\left\langle\sigma_{\rm aiso}\right\rangle\left\langle\sigma^{\rm ah}_{\rm aiso}\right\rangle}{\left.\partial^2 A^{\rm lat+qh}/\partial\alpha^2\right|_{\hat{\alpha}}},$$

where the anharmonic stress tensor is given by,

$$\begin{aligned}\left\langle\sigma^{\rm ah}_{\rm aiso}\right\rangle&=\left\langle\sigma_{\rm aiso}\right\rangle-\sigma^{\rm lat+qh}_{\rm aiso}\\&=\left\langle\sigma_{\rm aiso}\right\rangle-\frac{3\hat{\alpha}}{2V}\,\left.\frac{\partial A^{\rm lat+qh}}{\partial\alpha}\right|_{\hat{\alpha}}.\end{aligned} \tag{17a}$$

It may be possible to develop a HMA expression that yields $\langle\sigma^{\rm ah}_{\rm aiso}\rangle$ as a direct average, but we have not done so at this time.

Thus, only $\langle\sigma_{\rm aiso}\rangle$ is obtained from the AIMD data, while derivatives of $A^{\rm lat+qh}$ are computed from lattice dynamics. Similar to $\langle...\rangle_0$ averages, the stress anisotropy $\langle\sigma_{\rm aiso}\rangle$ is not directly measured using the DFT-el model; rather they are given through a reweighting technique described in the next section.

III. MODELING AND COMPUTATIONAL DETAILS

A. DFT models of iron

All computations are carried out using the non-spin polarized DFT method and the projector-augmented wave approach[66], as implemented in the Vienna *ab initio* simulation package (VASP)[67], version 5.3.5. The exchange-correlation functional is described by the widely used Perdew-Burke-Ernzerhof generalized-gradient approximation[68]. The k-points are generated using a Γ-centered Monkhorst-Pack mesh.

The basic features distinguishing the DFT-0 and DFT-el models are summarized in Table I; the DFT-0* system referenced there is discussed in the next section. As described in Sec. II C, we compute $A^{\rm ah}_0(T;\hat{\alpha})$ for the DFT-0 system using thermodynamic integration in temperature, excluding effects on the PES from electronic excitation and variation of α with T. To accelerate the calculations, the pseudopotential of this reference is chosen with the smallest number of valence electrons available (8 electrons). The DFT-el model, on the other hand, aims for maximum accuracy and uses 16 valence electrons, the most available within VASP. First-order Methfessel-Paxton smearing (with $\sigma=0.2$ eV) is used with the DFT-0 model, while Mermin's finite temperature extension of DFT[69] (using Fermi-Dirac statistics, with $\sigma=k_{\rm B}T_{\rm el}$) is used to account for the electronic thermal excitation in the DFT-el model.

The energy cutoff and k-mesh parameters for both the DFT-0 and DFT-el systems are selected to guarantee that the energy is converged for the conditions where they are used, ensuring that the FE ultimately obtained is within a tolerance of 2 meV/atom. These choices are summarized in Table II.

B. Low/high-accuracy reweighting

In principle, all the ensemble averages given by or appearing in Eqs. (8), (10), (16), and (17) should be sampled/measured using well-converged AIMD simulations of either the DFT-0 model, to get $\left\langle U_0^{\rm ah}\right\rangle_0$ and $A_{0\to{\rm el}}^{\rm ah}$, or the DFT-el model, to get $\delta\alpha^{\rm cor}$ and $\langle\sigma_{\rm aiso}\rangle$. However, running AIMD long enough to collect meaningful statistics is not presently feasible. To give a sense of the CPU computation cost, each AIMD step for the DFT-0 and DFT-el models takes about 10 and 30 hours, respectively, using one 12-core processor. A solution around this problem is to run AIMD with cheaper DFT parameters to generate the configurations, from which snapshots are taken to perform well converged DFT calculations. We label this system DFT-0*, having DFT modeling parameters as given in Tables I and II. A rigorous reweighting technique is then applied to these configurations to fix the inaccuracy introduced by using DFT-0* configurations.

Using this approach, $\left\langle U_0^{\rm ah}\right\rangle$ (Eq. (8)) and $A_{0\to{\rm el}}^{\rm qh+ah}$ (Eq. (10)) quantities are transformed into the following reweighted averages,

$$\left\langle U_0^{\rm ah}\right\rangle_0 = \left\langle U_0^{\rm ah}\times\mathcal{W}_0\right\rangle_{0^*}, \tag{18}$$

and

$$A_{0\to{\rm el}}^{\rm qh+ah} = -k_{\rm B}T\ln\left\langle e^{-\beta(\Delta U-\Delta U_0)}\times\mathcal{W}_0\right\rangle_{0^*}, \tag{19}$$

where $\mathcal{W}_0$ is a reweighting function joining DFT-0* and DFT-0 models (with potential energies U_{0^*} and U_0, respectively); specifically:

$$\mathcal{W}_0 \equiv \frac{e^{-\beta(U_0-U_{0^*})}}{\left\langle e^{-\beta(U_0-U_{0^*})}\right\rangle_{0^*}}. \tag{20}$$

Similarly, the average anisotropic stress tensor $\langle\sigma_{\rm aiso}\rangle$ of the DFT-el model is transformed into,

$$\langle\sigma_{\rm aiso}\rangle = \langle\sigma_{\rm aiso}\times\mathcal{W}\rangle_{0^*}, \tag{21}$$

where $\mathcal{W}$ is a reweighting function joining DFT-0* and DFT-el models, and is given by

$$\mathcal{W} \equiv \frac{e^{-\beta(U-U_{0^*})}}{\left\langle e^{-\beta(U-U_{0^*})}\right\rangle_{0^*}} \tag{22}$$

Although mathematically correct as written, a few considerations must be taken into account when evaluating these reweighted averages in practice. First, notice that the denominators of both $\mathcal{W}_0$ and $\mathcal{W}$ functions are ensemble averages themselves; therefore, two ensemble averages are evaluated to get the reweighted quantity. Since both averages are sampled from the same set of configurations, the covariance between them has to be considered when evaluating uncertainty of the reweighted averages. Second, due to the extensive nature of the potential energy, evaluating the exponentials can cause either round-off or overflow errors. A trick around this problem is to always measure the potential energy difference between systems relative to the minimum difference measured from all configurations — taking this difference, clearly, does not change the average itself. Third, the ensemble averages are evaluated by performing well-converged DFT single-point calculations (using DFT-0 and DFT-el specifications) on samples taken from the AIMD trajectory of the DFT-0* model and then averaged.

Grabowski *et al.*[70] previously proposed and implemented "upsampling," which is also based on the idea of sampling configurations of an inexpensive unconverged DFT model to yield ensemble averages for a more expensive and more accurate DFT model. While having this feature in common with upsampling, the approach used here differs from it in significant ways. No approximations are introduced in the reweighting equations (18), (19), and (21), while the upsampling method is based on a first-order approximation of the full FE perturbation expression. Therefore, its applicability is limited to cases where the sampled (reference) and measured (target) systems are "close" to each other (i.e. small energy-difference fluctuations). Grabowski *et al.* provide diagnostics to help detect such problems.

The reweighting approach advocated here should be more robust with respect to this issue, but still, failure due to poor overlap of the DFT-0* and target-system (DFT-0 or -el) configurations can happen in principle. Problems can be identified by examining a plot of $\mathcal{W}/\mathcal{W}^{\rm max}$ through the course of the simulation, where $\mathcal{W}^{\rm max}$ is the largest value of $\mathcal{W}$ observed in the run. If performing well, this chart will show that this ratio is non-negligible (say, greater than 0.1) for most of the configurations (see Figs. S1 and S2 of the Supplemental Material[71] showing results of the present calculations). If only one or two configurations dominate, this is indicative of poor sampling of the target by DFT-0*. Of course, the absence of such indicators does not guarantee that there is no problem, because it is possible that there are much higher-weight target-system configurations that are completely missed by the DFT-0*-system sampling. This is a pernicious problem with single-direction FE perturbation in general[17], but in the present application the risks are made smaller by the fundamental similarity of the DFT-0* and target systems.

C. Computational details

A single hcp isochore, $V = 7.0$ Å^3/atom, is used throughout this work. A two-atom-basis primitive unit cell is used to compute the lattice energy, while a $3\times3\times3$ supercell ($N = 54$ atoms) is used to compute the quasi-harmonic and anharmonic FE contributions. Larger supercells — $4\times4\times4$ ($N = 128$) and $5\times5\times5$ ($N = 250$) — are used to determine the finite-size effects in the quasi-harmonic contribution(Sec. IV D). For each supercell, the qh FE is computed via a Γ-point q-mesh (yielding $3(N-1)$ phonon frequencies $\omega^{(j)}$ used in Eq. (5)); the use of larger q-meshes for each N (Fourier interpolation) was

TABLE I: Description of the models. More detailed specifications of "DFT quality" are provided in Sec. III and Table II.

Model	$T_{\rm el}$	Smearing method	Valence electrons	DFT quality
DFT-0*	0K	Methfessel-Paxton	8 ($4s\ 3d$)	low
DFT-0				high
DFT-el	T	Fermi-Dirac	16 ($3s\ 3p\ 4s\ 3d$)	high

TABLE II: DFT energy cutoff and $k_x \times k_y \times k_z$ mesh parameters (presented for only k_x, as $k_x = k_y = k_z$) used to obtain FE accuracy within 2 meV/atom. The 8/6 input means that values of $k_x = 8$ and 6 were used with $T \leq 2000$ and > 2000 K, respectively.

Parameter	$U^{\rm lat}$ (DFT-el)	$A^{\rm qh}$ (DFT-el)	AIMD (DFT-0*)	Snapshots to: DFT-0	Snapshots to: DFT-el
$E_{\rm cut}$(eV)	500	600	250	400	500
k_x	20	8	2	8/6	8/6

not found to accelerate convergence to the infinite-system limit. The quasiharmonic FE is computed using the frozen-phonon method[18], as implemented in Phonopy[72] (version 1.9.0.1), with VASP used to compute forces.

The AIMD simulations are performed using Born-Oppenheimer dynamics in the standard canonical (NVT) ensemble, with the temperature controlled using a Langevin thermostat[73] with a friction coefficient of 10 ps^{-1} (other values do not show statistically different results). A time step of 4.0 fs is chosen (see Sec. IV A for justification) to run the AIMD simulations and a duration of 5 ps (after 1 ps of equilibration) is used to collect data. Five temperatures are examined, from 1000 to 5000 K, with a step of 1000 K.

At each temperature, 50 snapshots from the AIMD trajectory are taken to compute the reweighted expressions (Eqs. (18), (19), and (21)) using the well-converged DFT-0 and DFT-el specifications (see Table II; note that more k-mesh points are used at lower temperature). Although the correlation in these snapshots is small (≈ 20 %), block averaging (using 10 blocks) is employed to get an accurate estimate of uncertainties (stochastic errors).

IV. RESULTS AND DISCUSSION

A. AIMD time-step size

A critical parameter for MD simulations is the size of the integrator time-step Δt — large Δt can introduce inaccuracy that is larger than the stochastic uncertainty; at the same time, the sampling becomes inefficient if a very small value is used. Special to AIMD simulations, however, is the effect of Δt on the number of self-consistent field (scf) iterations. For AIMD codes (e.g. VASP) that extrapolate the wave functions and/or charge density

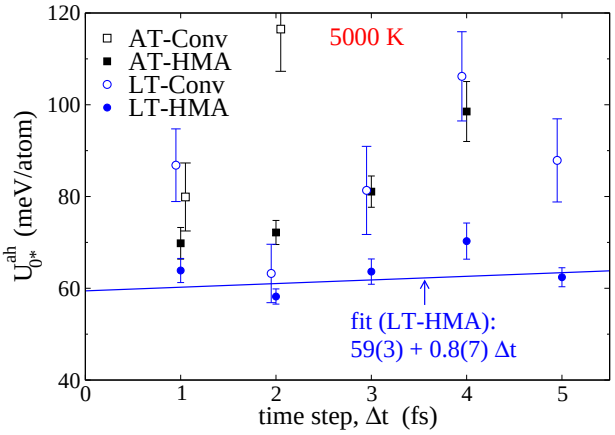

FIG. 1: (Color online) Convergence of the anharmonic energy (using the DFT-0* model) with respect to AIMD time-step size at 5000 K, using AT/LT thermostats and Conv/HMA averaging methods.

from one configuration to the next, using large Δt increases the deviation between these two configurations and hence the scf calculation becomes slower. Therefore, a careful testing has to be done before collecting data in order to ensure that the inaccuracy introduced by Δt is within some tolerance and, at the same time, the AIMD is efficient in terms of scf iterations. Moreover, for NVT simulations a thermostat must be used to control the temperature. The choice of the thermostat type can affect the level of inaccuracy introduced by Δt. For our case, we investigate the effect of using Andersen[74] (AT) and Langevin[73] (LT) thermostats on inaccuracy (Nosé-Hoover is avoided due to ergodicity reasons associated with quasiharmonic behavior[16]).

We use the anharmonic energy (based on the DFT-0* model, for demonstration) to show the effect of Δt on its accuracy, at the maximum temperature (5000 K) visited in this work — similar qualitative behaviour (not shown) was observed with the anisotropic stress tensor. The effect of the averaging formulas of $U^{\rm ah}$, i.e. Conv (Eq. (7)) or HMA (Eq. (8)), is also considered, and results are presented in Fig. 1. LT (with both Conv and HMA) shows a much smaller (statistically flat) dependence on Δt, compared to AT. On the other hand, the uncertainty does not show strong dependence on the thermostat type (for a given averaging method), but it is strongly dependent on the form of the average, with HMA about seven times more precise than Conv (the improvement increases with decreasing temperature[46]). In addition to its low uncertainty, the HMA formulation suppresses the effect of Δt on accuracy (especially with AT), allowing for use of larger Δt for a given thermostat.

For the purpose of computing the anharmonic FE using HMA-TI, it is interesting to investigate how Δt affects the accuracy of measuring the TI integrand (i.e. $U^{\rm ah}/T^2$). Repeating the above analysis with other temperatures (1000 and 3000 K; not presented here) shows that the slope of $U^{\rm ah}/T^2$ versus Δt is (statistically) independent of T. Hence, the inaccuracy in the anharmonic

FE has a similar magnitude to that of $U^{\rm ah}$. The LT is, then, still insensitive to Δt, while it varies as T^2 if AT is used. Therefore, we use the Langevin thermostat with the HMA method (LT-HMA) to collect data throughout this work. Although the LT-HMA data show a statistically flat variation with respect to Δt, we use a value of 4.0 fs to avoid lack of scf convergence. The inaccuracy introduced by AT, if a value of 4.0 fs is used, would be larger than $\approx$ 40 meV/atom; which is greater than the tolerance limit of this work (2 meV/atom).

B. Equilibrium c/a-ratio

Figure 2 shows the variation of the equilibrium c/a-ratio with T, using both minimization of the lat+qh FE with respect to α and with anharmonicity included through the correction technique as described in Sec. II E (Eq. (16)). For the latter, as mentioned in II E the simulated value of c/a was set to be that from lat+qh at 6000 K ($\hat{\alpha} = 1.6267$). As expected, both approaches agree at low T and start to deviate at high T, where anharmonicity effects become important. To give an analytical description, the full data are fitted using a 2$^{\rm nd}$-order polynomial in T. To force the function to go to the known value at 0 K (1.5925, given from the lattice energy), the fit was performed on $\beta\left[\alpha\left(T\right)-\alpha\left(0\right)\right]$ (Fig. S3 in the Supplemental Material shows the fitted data. All fitting details for the rest of this paper are found in the Supplemental Material). The fitting function is given by,

$$\alpha_{\rm eq}\left(T\right) = 1.5925 + 1.61\times10^{-6}T + 7.40\times10^{-10}T^2 - 2.06\times10^{-14}T^3. \quad (23)$$

The monotonically increasing behavior of the equilibrium c/a-ratio is in good agreement with previous theoretical[75] and experimental (at nearby densities)[76,77] results.

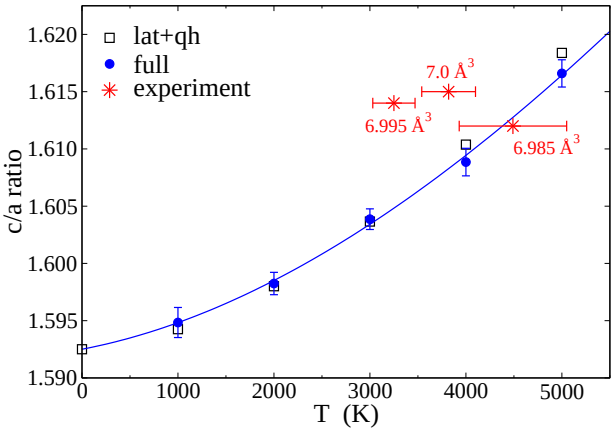

FIG. 2: (Color online) Variation of hcp c/a axial ratio with temperature using lattice+quasiharmonic components (lat+qh) and including anharmonicity (full) using Eq. (16). The line is a 2$^{\rm nd}$-order polynomial fit of the full $\beta\left[\alpha\left(T\right)-\alpha\left(0\right)\right]$ data, constrained to go to $\alpha\left(0\right)$ at 0 K (1.5925). The red points are experimental data for the indicated volumes per atom[76].

C. Free energy

In this section, we present the variation of each component of Eq. (4) with T, and express the variation using analytical functions fitted to the results.

1. *Lattice energy*

Figure 3 (a) shows the temperature dependence of the lattice energy $U^{\rm lat}\left(T;\alpha_{\rm eq}\left(T\right)\right)$ as a difference from that at 0 K. As mentioned above, the two sources of the T-dependence are (1) the electronic excitation associated with metallic systems; (2) the variation of $\alpha_{\rm eq}$ along T. To characterize this variation, a 2$^{\rm nd}$-order polynomial function is fit to the data. In order to force the lattice energy to go to the known 0 K value, the fitting is performed on $\beta\left[U^{\rm lat}\left(T\right)-U^{\rm lat}\left(0\right)\right]$. The lattice energy (in meV/atom) from this fit is given by,

$$U^{\rm lat}(T;\alpha_{\rm eq}) = -6501.80 - 5.77\times10^{-4}T - 8.11\times10^{-6}T^2 - 3.90\times10^{-10}T^3, \quad (24)$$

where T is in K. The deviation of the data from the fitting function is less than 0.2 meV/atom.

2. *Quasiharmonic FE*

Figure 3 (b) shows the variation of the quasiharmonic contribution $A^{\rm qh}\left(T;\alpha_{\rm eq}(T)\right)$ with T. Although we have an analytical formula for this contribution (Eq. (5)), the phonon frequencies $\omega^{(j)}$ of DFT-el model are T-dependent (due to electronic excitation) and hence a fitting is still required. However, most of the qh FE of the DFT-el model originates in the qh FE of the respective 0 K PES (i.e., $A^{\rm qh}\left(T;T_{\rm el}=0\right) = c_1T + c_2T\ln T$, with c_i independent of T), the fitting is more efficient when performed on the difference $A^{\rm qh}\left(T;T_{\rm el}=T\right) - A^{\rm qh}\left(T;T_{\rm el}=0\right)$. The fitted function is then added to that 0 K quasiharmonic FE to get the target $A^{\rm qh}$ representation. The actual fitting, however, is done on the difference divided by T to constrain the difference to be zero at 0 K, from which the qh FE (in meV/atom) is given by (with T in K):

$$A^{\rm qh}(T;\alpha_{\rm eq}(T)) = A^{\rm qh}\left(T;T_{\rm el}=0,\alpha_{\rm eq}(0)\right) - 1.30\times10^{-3}T + 1.60\times10^{-6}T^2 - 9.70\times10^{-10}T^3 + 7.04\times10^{-14}T^4, \quad (25a)$$

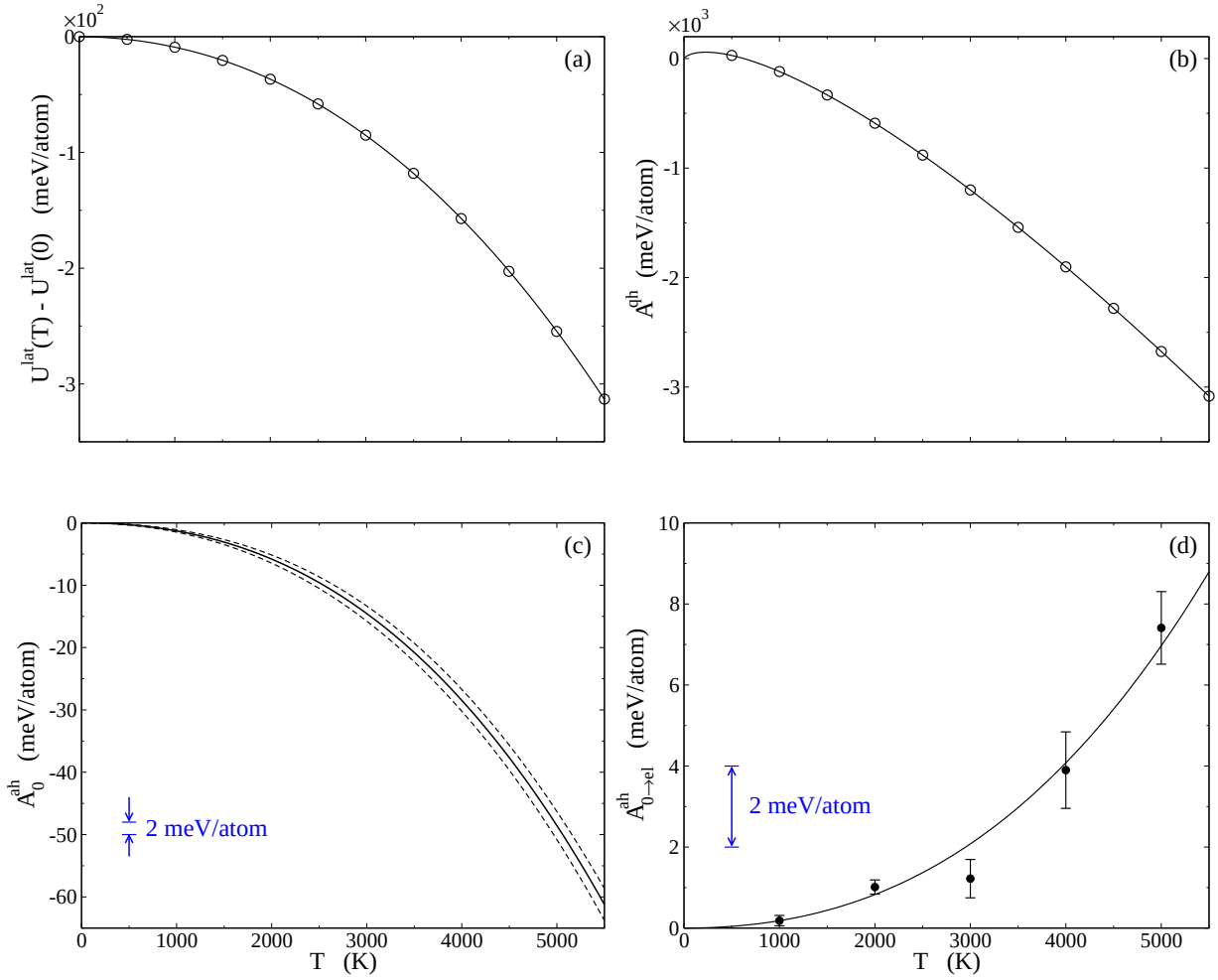

FIG. 3: Variation of the Helmholtz FE contributions with temperature. (a) Lattice energy, relative to that at 0 K; the line is obtained from fitting $\beta\left[U^{\rm lat}\left(T\right)-U^{\rm lat}\left(0\right)\right]$ to force the data to go to zero at 0 K. (b) Quasiharmonic FE; the line is obtained from fitting $\beta\left[A^{\rm qh}\left(T;T_{\rm el}=T\right)-A^{\rm qh}\left(T;0\right)\right]$ to force the data to go to zero at 0 K. (c) Anharmonic FE of DFT-0 model (with $c/a=\hat{\alpha}$) obtained from linear fitting of the HMA data (Fig. 4); dashed lines are the uncertainty limits. (d) Anharmonic FE correction between DFT-0 and DFT-el models; the line is obtained from fitting $\beta^2 A^{\rm ah}_{0\to\rm el}$ to force both the data and slope to go to zero at 0 K. Uncertainties are based on 68% confidence limits. See Supplemental Material for fitting details.

where

$$A^{\rm qh}\left(T;T_{\rm el}=0,\alpha_{\rm eq}(0)\right)=1.63478\,T-0.25373\,T\,\ln T \tag{25b}$$

as obtained using Eq. (5), with the T-independent frequencies computed from the $T_{\rm el}=0$ PES of the DFT-el model (but using Methfessel-Paxton smearing). The deviation of the data from the fitting function is less than 0.1 meV/atom.

3. *Anharmonic FE*

For the anharmonic FE contribution, the TI integrand (or, $U_0^{\rm ah}/\hat{T}^2$) variation with $\hat{T}$ is the quantity to investigate in detail. Figure 4 shows the change of the integrand with temperature, using both Conv and HMA averaging methods. All AIMD simulations were performed using $\Delta t=4.0$ fs with the Langevin thermostat to control the temperature (see Sec. IV A). There are four main observations to make from this plot. First, the Conv and HMA data are not consistent; however, this is not unexpected based on Fig. 1, which shows that both methods agree (statistically) at smaller Δt but not at $\Delta t=4$ fs. Second, the HMA data have much smaller stochastic uncertainty relative to Conv method ($\approx$ 4-12 $\times$ smaller; i.e. $\approx$ 15-150$\times$ CPU time saving, depending on T and the method). Third, for the HMA method, the uncertainty from the reweighted DFT-0 model is larger than that of the DFT-0* model ($\approx$ 1-3$\times$, depending on T). This could be attributed to the different important configurations visited by the DFT-0 and DFT-0* models, which are magnified by the exponential reweighting functions (Eqs. (20) and (22)). Finally, from the point of view of

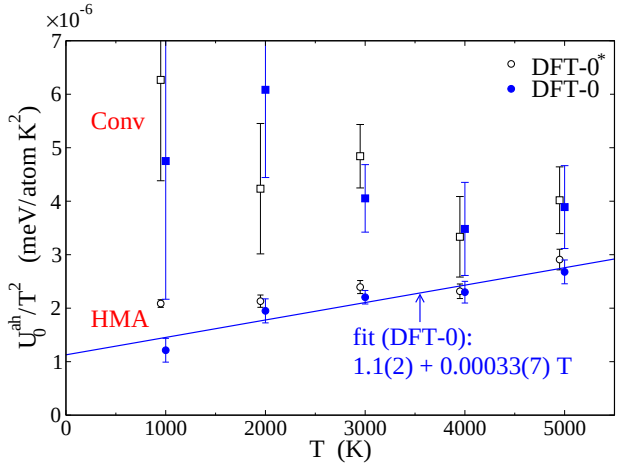

FIG. 4: (Color online) Anharmonic FE integrand of DFT-0*/0 models, using the Conv/HMA averaging methods, with the temperature controlled using the Langevin thermostat. Values for 0* are shifted slightly to the left to allow them to be distinguished from the DFT-0 values. Uncertainties are based on 68% confidence limits.

accuracy, using the well converged DFT-0 model is important (especially at low temperatures) to compute the integrand with the HMA method. The inaccuracy introduced by directly (i.e. with no reweighting) using DFT-0* to compute the anharmonic FE is about 10 meV/atom at 5000 K. On the other hand, the inaccuracy introduced by using the Conv method (with/without reweighting) is over 50 meV/atom.

We observe that the convergence of the integrand with respect to the DFT k-point density is T-dependent: a denser mesh is needed as temperature decreases. Figure S7 in the Supplemental Material shows this trend, and provides the basis for selection of different k-point settings for low vs. high temperature ranges (see Table II for specific values).

Figure 3 (c) shows the anharmonic FE of the DFT-0 model, obtained from integrating the linearly fitted HMA data (Fig. 4). The fitting function is given by,

$$A_0^{\rm ah}(T;\hat{\alpha}) = -1.10\times10^{-6}T^2 + 1.65\times10^{-10}T^3. \quad (26)$$

The stochastic uncertainty obtained from fitting (dashed lines) increases from zero (at 0 K) to ≈ 2 meV/atom (at 5000 K), which is just within our FE tolerance range.

The anharmonic FE correction $A^{\rm ah}_{0\to\rm el}$ due to using DFT-0 instead of DFT-el model (Eqs. (10) and (19)) is depicted in Fig. 3 (d); the convergence of this contribution with respect to the k-mesh density is presented in Fig. S8 of the Supplemental Material. By definition, both the correction and its slope (since the leading term of the anharmonic FE is T^2) must go to zero at 0 K; hence, the fitting is performing on the data divided by T^2 to get this behavior. Using linear fitting, we obtain the following fitted function (in meV/atom),

$$A^{\rm ah}_{0\to\rm el}(T;\hat{\alpha}) = 1.60\times10^{-7}T^2 + 2.39\times10^{-11}T^3, \quad (27)$$

where T is in K. At 5000 K, the data show that the anharmonic FE inaccuracy introduced by not using the DFT-el model is around 8 meV/atom, which exceeds our FE tolerance limit. Hence, this suggests the importance (at least for our application) of fully considering the DFT-el model to capture the anharmonic behavior of iron at such high pressure. The effect, however, of ignoring electronic excitation in $U^{\rm lat}$ and $A^{\rm qh}$ is more critical as shown in Fig. S9 of the Supplemental Material, where the inaccuracy associated with ignoring this effect is $\approx$ 50-300 meV/atom (depending on T and measured quantity).

Finally, we consider the anharmonic FE correction $A^{\rm ah}\left(T;\hat{\alpha}\to\alpha_{\rm eq}\right)$ due to not using the equilibrium c/a. Based on Eq. (17), this correction is proportional to the full, $\langle\sigma_{\rm aiso}\rangle$, and anharmonic, $\langle\sigma^{\rm ah}_{\rm aiso}\rangle$, stress anisotropy. Figure S10 in the Supplemental Material presents the variation of both components with temperature at fixed $c/a=\hat{\alpha}$. The data suggest that $\langle\sigma^{\rm ah}_{\rm aiso}\rangle$ is statistically zero and, accordingly, the $A^{\rm ah}\left(T;\hat{\alpha}\to\alpha_{\rm eq}\right)$ correction is negligible. On the other hand, although the effects of the c/a ratio on lattice and quasiharmonic contributions are already included in our $U^{\rm lat}$ and $A^{\rm qh}$ estimates, we explicitly demonstrate those effects in the Supplemental Material (Fig. S11), but with $\hat{\alpha}$ set equal to $\alpha_{\rm eq}(0)$ such that the corrections start from zero at 0 K. The effect (especially with the quasiharmonic correction) is non-negligible, compared to our FE tolerance, and increases with temperature. It is not uncommon to see a fixed c/a ratio used for these calculations, yielding a FE that differs markedly from the equilibrium value.

D. Finite-size effects

As shown by our earlier work with classical models[46,48,53], the anharmonic FE has much smaller finite-size effects compared to the quasiharmonic part. The current work shows that this conclusion is still valid for DFT-type models (at least for iron). Figure 5 presents the anharmonic FE from two system sizes ($N=54$ and 128), using the DFT-0 model with $c/a=\hat{\alpha}$. Although this is not the actual anharmonic FE of the target system (i.e., DFT-el with $\alpha_{\rm eq}$), the model is still a representative DFT PES that can serve in demonstrating the finite-size effects. The results show that the difference in the anharmonic FE between the two system sizes is no larger than our FE tolerance, even at the highest temperature simulated (5000 K), and in fact at all temperatures is smaller than the uncertainty in the difference.

In contrast, the DFT-el quasiharmonic contribution, at 5000 K shows a much stronger N-dependence, as depicted for three system sizes ($N=54, 128$ and 250) in Fig. 6. As recommended by Hoover[78], the data are presented as a difference from $k_{\rm B}T\ln N/N$, which he de-

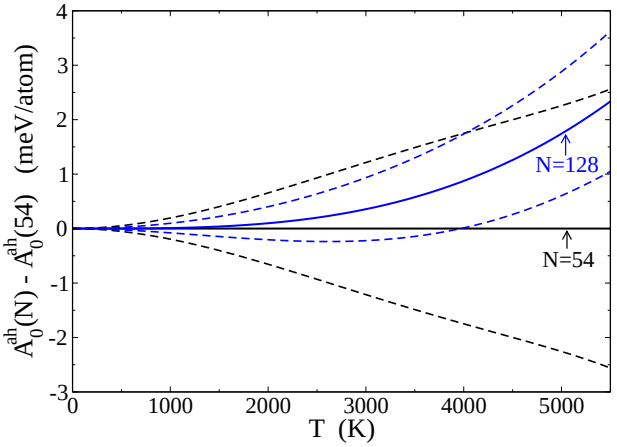

FIG. 5: (Color online) Anharmonic finite-size effects of the DFT-0 model, using $c/a = \hat{\alpha}$. The dashed lines delineate the 68% confidence intervals.

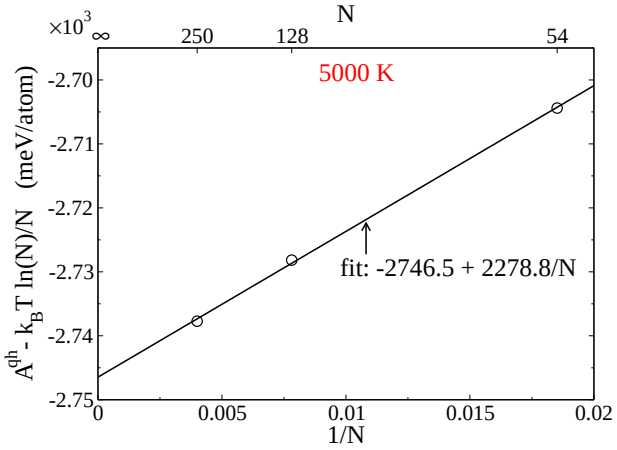

FIG. 6: Quasiharmonic finite-size effects of the DFT-el model at 5000 K, using $c/a = \alpha_{eq}(5000\,\mathrm{K}) = 1.6164$. The $-k_B T \ln N/N$ term is added to reduce curvature in the data (see text for details).

rived as the leading N dependence of A^{qh} — although Hoover's development is based on a simple model with only nearest-neighbor interactions, the near-linear behavior of our data suggest that this conclusion is valid here as well. Clearly, the finite-size effect (reflected in the slope of the data) is quite large in comparison to the tolerance. For example, the difference in the quasiharmonic FE between $N = 54$ and 128 is about 40 meV/atom, and between 54 and ∞ is about 70 meV/atom. This effect is about 2% of the total A^{qh} value, and is as large as the anharmonic contribution itself. The finite-size effects are temperature-dependent due to the effect of electronic excitations on the phonon frequencies — a behavior that does not exist with systems modeled using a 0 K PES. The degree of variation of the quasiharmonic FE with N differs with temperature, suggesting that the finite-size analysis (i.e. Fig. 6) has to be repeated at each temperature of interest. This behavior is demonstrated in Fig. S12 of the Supplemental Material, which shows the N dependence of the nontrivially T-dependent part of A^{qh} at 4000 and 5000 K.

These findings suggest that the total FE in the thermodynamic limit can be estimated by extrapolating only the quasiharmonic FE, instead of the full (qh+ah). For DFT-type calculations, this is of great importance because performing AIMD with large system sizes is not (at least for many systems) tractable using the current computing power.

V. CONCLUSIONS

We have introduced an efficient and robust framework for measuring the anharmonic FE of crystalline metallic systems, in the thermodynamic limit, using AIMD simulations, with full inclusion of electronic excitation and effect of geometry. The approach is applied to the high-pressure (≈ 290 GPa) hcp-phase of iron up to 5000 K. The computational motivation for this choice (in addition to the geophysical interest) is twofold: (1) at such dense states, a high level of DFT theory is needed to model iron, which is computationally very demanding; (2) the FE difference between different candidate structures of iron is small (tens of meV/atom) for the range of conditions of interest. Therefore, achieving affordable anharmonic FE computations of this system is of high interest.

The calculated FE as a function of temperature for the 7.0 Å^3/atom isochore is encapsulated in Eq. (4); the temperature dependences of the components are given by the fits reported throughout Sec. IV C, which are convenient representations of the results of the calculations performed in this work.

Some key elements of the framework that allow for calculation of high-accuracy results include:

1. Using the recently developed HMA-TI approach[46–48] to determine the baseline temperature dependence of the anharmonic FE, providing results with order(s) of magnitude CPU speed-up (≈ 15-150×, compared to conventional TI).

2. Careful attention to the effect of thermostat on convergence with respect to AIMD integration time step, wherein it was found that the Langevin thermostat with the HMA-TI method introduced negligible time-step dependence, compared to the Andersen thermostat — while a step size of 4 fs with the Langevin thermostat was statistically accurate, a much smaller value (≈ 0.5 fs) is needed for the Andersen thermostat to yield the same level of accuracy.

3. The efficiency of AIMD sampling was accelerated via a reweighting technique, in which the sampling is drawn from a low-level DFT model (DFT-0*), from which a higher level of DFT theory (DFT-

0 and DFT-el) is performed on several configurations from AIMD samples. The approach is robust, such that the accuracy we get eventually is that of the DFT models, with a computational speed-up of around 20-30×, compared to directly sampling the target models.

4. The difficulty associated with applying a TI method to a model that has T-dependence of the PES (due to electronic excitation) and geometry (c/a ratio in this case) along the path is treated in a simple perturbative manner.

5. We treat finite-size effects of the FE components differently, extrapolating quasiharmonic FE contributions to the thermodynamic limit, while evaluating the anharmonic contribution using a small system, because it is weakly dependent on system size.

An important technical advantage of the HMA-TI approach is that it can be directly implemented to typical molecular simulation packages without modifying the sampling potential. This is not the case with other methods[70,79] in which the sampling potential is modified along the path, which is not a trivial task by itself.

A key element of the scheme is integration in temperature from a quasiharmonic reference at $T = 0$ K to the conditions of interest. Potential complications such as imaginary phonon frequencies of the harmonic reference, and concern about nuclear quantum effects were discussed briefly in Secs. II. In this respect it is worth noting that the HMA-TI framework for efficient computation of properties (Eq. (8) in particular) does not require that the harmonic system be dynamically stable. Hence, it can be used even in these cases to speed the mapping of FE versus temperature (and/or density) (via thermodynamic integration) once the FE is obtained by some means at a single dynamically stable thermodynamic state point. On the other hand, its need for a clear assignment of atoms to lattice sites will complicate application of HMA to systems exhibiting frequent diffusion events (such as observed in bcc iron[80]).

As with prior efforts to compute accurate free energies of iron at extreme conditions using AIMD, we have not incorporated magnetic behaviors in our calculations. Iron in the hcp form is undoubtedly paramagnetic at these conditions, and among the iron allotropes it has the weakest magnetic behavior. Moreover, spin-polarized calculations that we performed with VASP did not show a net magnetic moment or any other effects relevant to the FE at the volume and temperatures examined here. On the other hand, a recent report[50], based on a simple classical model and excluding lattice vibrations, suggests that at extreme conditions the magnetic and thermodynamic properties of iron can be substantially influenced by longitudinal spin fluctuations, and that DFT as conventionally applied does not capture this behavior. This remains then an unquantified potential inaccuracy in our calculations. If needed, it should be possible to capture the effect of this phenomenon on the FE perturbatively at each temperature, starting from the results developed here and using emerging methods for quantifying combined electronic-magnetic-vibrational effects[81–83].

The computational framework developed here can be used as a basis for calculation of regions of stability for various phases of iron at high pressure and temperature, solely based on *ab initio* methods. This would require repeating the isochoric calculations with different candidate structures, and observing where the Helmholtz FE curves cross. These points do not represent coexistence conditions, but they do indicate a change of the stable form for the given density. A more complete mapping of the FE surface, examining multiple isochores for each structure, can be used to compute the phase boundaries while also providing values of the pressure. With the general structure of the phase diagram established, details can be filled in by using methods for tracing coexistence lines[84,85], in conjunction with HMA methods for calculation of other properties[46]. Generation of an accurate and comprehensive phase diagram for pure iron in this manner would establish a suitable starting point to launch calculations of comparable accuracy for iron-rich compounds relevant to the Earth's inner core.

ACKNOWLEDGMENTS

This work was supported by an IMPACT grant from the University at Buffalo (UB), and a grant to EZ from the U.S. National Science Foundation (DMR-1505817). Computational support was provided by the UB Center for Computational Research (CCR). We deeply thank Tomas Bucko, James Hooper, and Andrew Shamp for their inputs and helpful comments during this work.

* Electronic mail: kofke@buffalo.edu

[1] S. M. Woodley and R. Catlow, Nat. Mater. **7**, 937 (2008).
[2] J. C. Schön, K. Doll, and M. Jansen, Phys. Status Solidi B **247**, 23 (2010).
[3] G. Rossi and R. Ferrando, J. Phys.: Condens. Matter **21**, 084208 (2009).
[4] Y. Wang and Y. Ma, J. Chem. Phys. **140**, 040901 (2014).
[5] C. J. Pickard and R. J. Needs, Phys. Status Solidi B **246**, 536 (2009).
[6] B. C. Revard, W. W. Tipton, and R. G. Hennig (Springer Berlin Heidelberg, 2014) pp. 1–42.
[7] A. R. Oganov, ed., *Modern Methods of Crystal Structure Prediction* (John Wiley & Sons, 2010).
[8] D. J. Wales, *Energy Landscapes: Applications to Clusters, Biomolecules and Glasses* (Cambridge: Cambridge University Press, 2003).
[9] E. Zurek, in *Reviews in Computational Chemistry*, Vol. 29, edited by K. B. Lipkowitz (John Wiley & Sons, Inc., Hobo-

ken, New Jersey, 2016) pp. 274–326.
[10] J. Badro, A. S. Côté, and J. P. Brodholt, Proc. Natl. Acad. Sci. USA **111**, 7542 (2014).
[11] L. Stixrude, E. Wasserman, and R. E. Cohen, J. Geophys. Res.: Solid Earth **102**, 24729 (1997).
[12] K. D. Litasov and A. F. Shatskiy, Russian Geology and Geophysics **57**, 22 (2016).
[13] L. Zhu, H. Liu, C. J. Pickard, G. Zou, and Y. Ma, Nat. Chem. **6**, 644 (2014).
[14] D. A. McQuarrie, *Statistical Mechanics* (University Science Books, 2000).
[15] P. A. Monson and D. A. Kofke, Adv. Chem. Phys. **115**, 113 (2000).
[16] D. Frenkel and B. Smit, *Understanding Molecular Simulation*, 2nd ed. (Academic Press, Inc., Orlando, FL, USA, 2001).
[17] D. A. Kofke, Fluid Phase Equilib. **228**, 41 (2005).
[18] M. T. Dove, *Introduction to Lattice Dynamics* (Cambridge University Press, New York, 2005).
[19] G. Kresse, J. Furthmüller, and J. Hafner, Europhys. Lett. **32**, 729 (1995).
[20] P. Giannozzi, S. de Gironcoli, P. Pavone, and S. Baroni, Phys. Rev. B **43**, 7231 (1991).
[21] A. M. Teweldeberhan, J. L. Dubois, and S. A. Bonev, Phys. Rev. Lett. **105**, 235503 (2010).
[22] A. B. Belonoshko, S. Arapan, and A. Rosengren, J. Phys. Condens. Matter **23**, 485402 (2011).
[23] L. T. Kong, Computer Physics Communications **182**, 2201 (2011).
[24] A. M. Teweldeberhan and DuBois, J. L. and Bonev, S. A., Phys. Rev. B **86**, 064104 (2012).
[25] D.-B. Zhang, T. Sun, and R. M. Wentzcovitch, Phys. Rev. Lett. **112**, 058501 (2014).
[26] Y. Hu and B. Wang, AIP Adv. **3** (2013).
[27] N. Antolin, O. D. Restrepo, and W. Windl, Phys. Rev. B **86**, 054119 (2012).
[28] O. Hellman, I. A. Abrikosov, and S. I. Simak, Phys. Rev. B **84**, 180301 (2011).
[29] O. Hellman, P. Steneteg, I. A. Abrikosov, and S. I. Simak, Phys. Rev. B **87**, 104111 (2013).
[30] O. Hellman and I. A. Abrikosov, Phys. Rev. B **88**, 144301 (2013).
[31] C. D. Barnes and D. A. Kofke, J. Chem. Phys. **117**, 9111 (2002).
[32] I. Errea, B. Rousseau, and A. Bergara, Phys. Rev. Lett. **106**, 165501 (2011).
[33] I. Errea, M. Calandra, and F. Mauri, Phys. Rev. Lett. **111**, 177002 (2013).
[34] I. Errea, M. Calandra, and F. Mauri, Phys. Rev. B **89**, 064302 (2014).
[35] B. Monserrat, N. D. Drummond, and R. J. Needs, Phys. Rev. B **87**, 144302 (2013).
[36] Z. Wu and R. M. Wentzcovitch, Phys. Rev. B **79**, 104304 (2009).
[37] Z. Wu, Phys. Rev. B **81**, 172301 (2010).
[38] Z. Wu, Earthquake Science **28**, 11 (2015).
[39] P. Souvatzis, O. Eriksson, M. I. Katsnelson, and S. P. Rudin, Comput. Mater. Sci. **44**, 888 (2009).
[40] D. Alfè, G. D. Price, and M. J. Gillan, Phys. Rev. B **64**, 045123 (2001).
[41] D. Alfe, G. D. Price, and M. J. Gillan, Phys. Rev. B **65**, 165118 (2002).
[42] L. Vočadlo, D. Alfè, M. J. Gillan, I. G. Wood, J. P. Brodholt, and G. D. Price, Nature **424**, 536 (2003).
[43] A. B. Belonoshko, P. I. Dorogokupets, B. Johansson, S. K. Saxena, and L. Koči, Phys. Rev. B **78**, 104107 (2008).
[44] L. Vočadlo, I. G. Wood, M. J. Gillan, J. Brodholt, D. P. D., G. D. Price, and D. Alfè, Phys. Earth Planet. Inter. **170**, 52 (2008).
[45] J. Bouchet, S. Mazevet, G. Morard, F. Guyot, and R. Musella, Phys. Rev. B **87**, 094102 (2013).
[46] S. G. Moustafa, A. J. Schultz, and D. A. Kofke, Phys. Rev. E **92**, 043303 (2015).
[47] A. J. Schultz, S. G. Moustafa, W. Lin, S. J. Weinstein, and D. A. Kofke, J. Chem. Theory. Comput. **12**, 1491 (2016).
[48] S. G. Moustafa, A. J. Schultz, and D. A. Kofke, J. Chem. Theory Comput. **13**, 825 (2017).
[49] S. Tateno, K. Hirose, Y. Ohishi, and Y. Tatsumi, Science **330**, 359 (2010).
[50] A. V. Ruban, A. B. Belonoshko, and N. V. Skorodumova, Phys. Rev. B **87**, 014405 (2013).
[51] A. S. Mikhaylushkin, S. I. Simak, L. Dubrovinsky, N. Dubrovinskaia, B. Johansson, and I. A. Abrikosov, Phys. Rev. Lett. **99**, 165505 (2007).
[52] L. Vočadlo, I. G. Wood, D. Alfè, and G. D. Price, Earth Planet. Sci. Lett. **268**, 444 (2008).
[53] T. B. Tan, A. J. Schultz, and D. A. Kofke, J. Chem. Phys. **132**, 214103 (2010).
[54] T. B. Tan and A. J. Schultz and D. A. Kofke, J. Chem. Phys. **135**, 044125 (2011).
[55] L. Vočadlo, J. Brodholt, D. Alfè, M. J. Gillan, and G. D. Price, Phys. Earth Planet. Inter. **117**, 123 (2000).
[56] J. Ihm, A. Zunger, and M. L. Cohen, J. Phys. C: Solid State Phys. **12**, 4409 (1979).
[57] S. K. Sharma, Solid State Commun. **149**, 2207 (2009).
[58] M. A. van der Hoef, J. Chem. Phys **113**, 8142 (2000).
[59] Y. Koyama, H. Tanaka, G. Gao, and X. C. Zeng, J. Chem. Phys **121**, 7926 (2004).
[60] J. A. Moriarty and J. B. Haskins, Phys. Rev. B **90**, 054113 (2014).
[61] C. Cazorla, D. Alfè, and M. J. Gillan, Phys. Rev. B **85**, 064113 (2012).
[62] H. Cui, Z. Zhang, and Y. Zhang, Geophys. Res. Lett. **40**, 2958 (2013).
[63] W. Zwanz, J. Chem. Phys **22**, 1420 (1954).
[64] C. Jarzynski, Phys. Rev. E **65**, 046122 (2002).
[65] T. B. Tan, A. J. Schultz, and D. A. Kofke, J. Chem. Phys. **133**, 134104 (2010).
[66] P. E. Blöchl, Phys. Rev. B **50**, 17953 (1994).
[67] G. Kresse and J. Furthmüller, Phys. Rev. B **54**, 11169 (1996).
[68] J. P. Perdew, K. Burke, and M. Ernzerhof, Phys. Rev. Lett. **77**, 3865 (1996).
[69] N. D. Mermin, Phys. Rev. **137**, A1441 (1965).
[70] B. Grabowski, L. Ismer, T. Hickel, and J. Neugebauer, Phys. Rev. B **79**, 134106 (2009).
[71] See Supplemental Material at [URL will be inserted by publisher] for information related to fitting procedures, quality-assurance measures, intermediate results not presented in the main text, and tables of the data appearing in the figures.
[72] A. Togo and I. Tanaka, Scr. Mater. **108**, 1 (2015).
[73] M. P. Allen and D. J. Tildesley, *Computer Simulation of Liquids*, Oxford Science Publ (Clarendon Press, 1989).
[74] H. C. Andersen, J. Chem. Phys **72**, 2384 (1980).
[75] C. M. S. Gannarelli, D. Alfe, and M. J. Gillan, Phys. Earth Planet. Inter. **152**, 67 (2005).
[76] T. Sakai, E. Ohtani, N. Hirao, and Y. Ohishi, Geophys. Res. Lett. **38** (2011).

[77] Fischer, R. A. and Campbell, A. J., American Mineralogist **100**, 2718 (2015).
[78] W. G. Hoover, J. Chem. Phys. **49**, 1981 (1968).
[79] D. Frenkel and A. J. C. Ladd, J. Chem. Phys **81**, 3188 (1984).
[80] A. B. Belonoshko, T. Lukinov, J. Fu, J. Zhao, S. Davis, and S. I. Simak, Nature Geoscience **10**, 312 (2017).
[81] F. Körmann, A. A. H. Breidi, S. L. Dudarev, N. Dupin, G. Ghosh, T. Hickel, P. Korzhavyi, J. A. Muñoz, and I. Ohnuma, Phys. Status Solidi B **251**, 53 (2013).
[82] I. A. Abrikosov, A. V. Ponomareva, P. Steneteg, S. A. Barannikova, and B. Alling, Curr. Opin. Solid State Mater. Sci. **20**, 85 (2016).
[83] F. Körmann, T. Hickel, and J. Neugebauer, Curr. Opin. Solid State Mater. Sci. **20**, 77 (2016).
[84] D. A. Kofke, J. Chem. Phys. **98**, 4149 (1993).
[85] D. A. Kofke, Adv. Chem. Phys. **105**, 405 (1999).